Theoretical study on ultrafast intersystem crossing of chromium(III) acetylacetonate

Hideo Ando[a], Satoru Iuchi[b], Hirofumi Sato[a,*]

[a] *Department of Molecular Engineering, Graduate School of Engineering, Kyoto University, Nishikyo-ku, Kyoto 615-8510, Japan*
[b] *Department of Complex Systems Science, Graduate School of Information Science, Nagoya University, Chikusa-ku, Aichi 464-8601, Japan*

Abstract

In the relaxation process from the $^4T_{2g}$ state of chromium(III) acetylacetonate, $Cr^{III}(acac)_3$, ultrafast intersystem crossing (ISC) competes with vibrational relaxation (VR). This contradicts the conventional cascade model, where ISC rates are slower than VR ones. We hence investigate the relaxation process with quantum chemical calculations and excited-state wavepacket simulations to obtain clues about the origins of the ultrafast ISC. It is found that a potential energy curve of the $^4T_{2g}$ state crosses those of the $^2T_{1g}$ states near the Franck-Condon region and their spin-orbit couplings are strong. Consequently, ultrafast ISC between these states is observed in the wavepacket simulation.

1. Introduction

Juban *et al.* have reported that $Cr^{III}(acac)_3$ in acetonitrile solution undergoes ultrafast intersystem crossing (ISC) from the initially-populated $^4T_{2g}$ excited state to the ^2E_g excited state at a rate of $k_{ISC} > 10^{13}$ s^{-1}, competing

*Corresponding author. Tel: +81 75 3832548. Fax: +81 75 3832799.
Email addresses: ando@riron.moleng.kyoto-u.ac.jp (Hideo Ando), iuchi@is.nagoya-u.ac.jp (Satoru Iuchi), hirofumi@moleng.kyoto-u.ac.jp (Hirofumi Sato)

with vibrational relaxation (VR) in the $^4T_{2g}$ state [1, 2]. In the same complex, it has also been proposed that back ISC may occur efficiently [3, 4]. These experimental studies indicate that ISC of $Cr^{III}(acac)_3$ occurs so efficiently that the relaxation process does not follow the conventional cascade model (i.e., $k_{ISC} < k_{VR}$). The detailed mechanism of this ultrafast ISC, however, has not been fully clarified. In general, elucidation of relaxation processes is still an important issue in transition-metal chemistry. For example, several concepts such as the cascade model and the heavy atom effect, which are applicable to most organic compounds, have recently been questioned [1, 2, 5, 6, 7, 8].

In order to understand the relaxation process of $Cr^{III}(acac)_3$, it is important to examine accurate potential energy surfaces of several excited electronic states involved in the process. However, investigating the full potential energy surfaces of multiple excited states is difficult in practice due to a relatively large number of vibrational degrees of freedom in transition-metal complexes. Many theoretical studies have therefore been investigating potential energy curves (PECs) along one or a few important coordinates [9, 10, 11, 12, 13, 14, 15]. Under this simplification, accurate wavefunction-based ab initio methods can be used to evaluate PECs and spin-orbit couplings (SOCs) [9, 10, 11]. In addition, dynamics studies using the Fermi's golden rule or wavepacket simulations are also feasible on the basis of the PECs and SOCs obtained [12, 13, 14, 15]. Consequently, those studies have provided valuable insights into excited state processes of transition-metal complexes.

Considering these experimental and theoretical studies, we aim to investi-

gate the ISC of $Cr^{III}(acac)_3$ after the $^4A_{2g} \rightarrow {}^4T_{2g}$ photoexcitation by focusing on structural relaxation of the $^4T_{2g}$ state. For this purpose, we prepare a one-dimensional path to connect two equilibrium geometries of the $^4A_{2g}$ and $^4T_{2g}$ states. Along the constructed path, the PECs and the SOCs are evaluated by means of wavefunction-based ab initio methods, namely the complete active space self-consistent field theory (CASSCF) and the multiconfigurational quasidegenerate perturbation theory (MCQDPT) calculations [16]. We then perform wavepacket simulations and discuss the ultrafast ISC to the intermediate $^2T_{1g}$ state in particular in order to find clues about the origins of the ultrafast relaxation process of $Cr^{III}(acac)_3$.

2. Ab initio calculations

2.1. Equilibrium geometries and linear reaction path

The geometries of $Cr^{III}(acac)_3$ were optimized with the DFT(B3LYP) method [17, 18, 19] for the $^4A_{2g}$ ground state and a Jahn-Teller stabilized $^4T_{2g}$ excited state within the C_2 point group. Note that each electronic state is specified by an irreducible representation of the O_h point group hereafter because the primary coordination sphere of the ground state geometry belongs approximately to this point group. An irreducible representation of the actual point group C_2 is also specified in parentheses when necessary. The ^2E_g geometry is stable but was not optimized because it is considered to be similar to the $^4A_{2g}$ geometry [20]. In all ab initio calculations, we employed the cc-pVTZ basis set [21] for the Cr atom and the cc-pVDZ basis sets [22] for the O, C, and H atoms. The

DFT(B3LYP) calculations and molecular visualization were carried out using the Gaussian 03 program suite [23] and Molekel 5.4 [24], respectively.

The equilibrium geometries of the ${}^4A_{2g}$ ground state and the lowest ${}^4T_{2g}({}^4A)$ excited state are summarized in Table 1. They are also visualized in Figure 1, where the two structures were positioned in the same xyz frame so as not to generate any linear or angular momentum [25, 26]. As listed in Table 1, all $\mathrm{Cr}-\mathrm{O}$ distances of the ${}^4A_{2g}$ geometry were estimated to be 1.975 Å, which is in good agreement with the experimental value of *ca.* 1.951 Å [27]. The electronic structures of the ${}^4A_{2g}$ and ${}^4T_{2g}({}^4A)$ states were characterized by $|d_{xy}d_{yz}d_{zx}|$ and $\left|d_{yz}d_{zx}d_{x^2-y^2}\right|$, respectively, indicating that the ${}^4A_{2g}\rightarrow{}^4T_{2g}({}^4A)$ excitation corresponds to a one-electron promotion from the t_{2g}-type d_{xy} to the e_g-type $d_{x^2-y^2}$ orbital [20]. Therefore, the optimized ${}^4T_{2g}$ geometry in Table 1 can be interpreted as a consequence of the Jahn-Teller distortion [20]: compared to the ${}^4A_{2g}$ geometry, four $\mathrm{Cr}-\mathrm{O}$ bonds in the xy plane are elongated because of the anti-bonding character of the $d_{x^2-y^2}$ orbital. The $\mathrm{Cr}-\mathrm{O}^2$ and $\mathrm{Cr}-\mathrm{O}^6$ bonds are longer than the $\mathrm{Cr}-\mathrm{O}^3$ and $\mathrm{Cr}-\mathrm{O}^5$ bonds probably because O^3 and O^5 belong to different acac ligands and the elongations of $\mathrm{Cr}-\mathrm{O}^3$ and $\mathrm{Cr}-\mathrm{O}^5$ induce ligand distortions. A dihedral angle between two front ligands in Figure 1 opens by 30° and ligand structures themselves remain little changed; in fact, displacement of any atom in each ligand was less than 0.1 Å.

As mentioned in Introduction, we focus on the ISC from the initially-populated ${}^4T_{2g}$ state to doublet states associated with the structural relaxation of the ${}^4T_{2g}$ state. We therefore prepare a reaction path to describe the structural change

from the $^4A_{2g}$ to the Jahn-Teller distorted $^4T_{2g}$ geometry obtained above. As such a path, we employed the linear reaction path S [25] which connects those two geometries with linear interpolation and extrapolation. In order to see the geometrical characteristics of this path, the displacement $\boldsymbol{K}$ vector in the Duschinsky rotation [26, 28],

$$\boldsymbol{K} = [\boldsymbol{M}\boldsymbol{L}^{^4A_{2g}}]^{\dagger}\Delta\boldsymbol{R}, \tag{1}$$

was calculated, where the $\boldsymbol{M}$ is a diagonal matrix including the atomic masses and the $\boldsymbol{L}^{^4A_{2g}}$ is a transformation matrix which diagonalizes the Cartesian Hessian of the $^4A_{2g}$ state to obtain the mass-weighted diagonal frequency matrix. The Duschinsky $\boldsymbol{K}$ vector is hence the normal-mode representation of the Cartesian displacement $\Delta\boldsymbol{R}$ vector between the two equilibrium geometries.

The resultant Duschinsky $\boldsymbol{K}$ vector is shown in Figure 2, where the absolute value of each $\boldsymbol{K}$ vector element was plotted with respect to the corresponding normal-mode frequency of the $^4A_{2g}$ state. As seen in Figure 2, only low-frequency modes have large $|\boldsymbol{K}|$ values or large displacements. The normal-mode analysis also showed that most of such low-frequency modes are mainly composed of displacements of the primary coordination sphere. For example, the normal mode whose displacement and frequency are 1.45 $\text{Å}\,\text{amu}^{1/2}$ and 182 cm^{-1} was assigned to $\text{Cr}-\text{O}$ stretch vibration. These results indicate that the obtained linear reaction path is mainly described by low-frequency modes which are responsible for the complex distortion motions. This seems to indicate that the reaction path employed here is a reasonable coordinate for investigating the ultrafast ISC, since the importance of the low-frequency modes, particularly the

$Cr-O$ stretch vibration (see Figure 4 in Ref. [4]), for the ultrafast ISC process has recently been discussed on the basis of both the experimental and DFT results [4].

2.2. Potential energy curves and spin-orbit couplings

The PECs of four low-lying quartet states, $^4A_{2g}$ and $^4T_{2g}$, and of five low-lying doublet states, ^2E_g and $^2T_{1g}$, were obtained along the linear reaction path using the GAMESS program suite [29]. Note that the similar PECs were obtained even when higher $^4T_{1g}$ states were included in the calculations. We employed the second-order MCQDPT method [16] so as to include both the static and dynamic electron correlation effects. In order to obtain the reference wave functions for the MCQDPT calculations, we first optimized the molecular orbitals using the state-averaged CASSCF$(3,5)$ method, where the active space $(3,5)$ means that three electrons are distributed among five Cr $3d$ orbitals. Then, we added the Cr $3s$ and $3p$ orbitals into the active space so as to take account of the strong intershell correlation effect [30] and performed the complete active space configuration interaction (CASCI) calculations with the resultant $(11,9)$ active space. It is noted here that the CASCI$(11,9)$/MCQDPT method would be comparable in accuracy with the CASSCF$(11,9)$/MCQDPT one because orbital optimization effect can be included to some extent even in the CASCI$(11,9)$ method [31, 32]. See the Supplementary Content for further discussion on the present active space selection. In the MCQDPT calculations, core electrons (i.e., Cr $1s$, $2s$, $2p$, C $1s$, and O $1s$) were not correlated and

an energy denominator shift of 0.02 hartree was introduced as intruder-state avoidance [33].

In order to examine the performance of the CASCI(11, 9)/MCQDPT calculations, we evaluated the averaged vertical excitation energies of $^4A_{2g}\rightarrow{}^2E_g$, $^4A_{2g}\rightarrow{}^2T_{1g}$, and $^4A_{2g}\rightarrow{}^4T_{2g}$ at the optimized $^4A_{2g}$ geometry. Note that the O_h assignment of each electronic state was performed by expanding the calculated wave function into the configuration state functions of the ligand field theory [34]. The three calculated values, 15609, 16892, and 18284 cm^{-1}, are in reasonable agreement with the corresponding CASPT2 excitation energies, 15540, 16530, and 16970 cm^{-1} [35], respectively, of the unsubstituted analog, $Cr^{III}(1,3\text{-propanedionate})_3$. In addition, the calculated values for the $^4A_{2g}\rightarrow{}^2E_g$ and $^4A_{2g}\rightarrow{}^4T_{2g}$ excitations are not significantly deviated from the experimental estimations, 13070 and 18233 cm^{-1}, respectively [35]. These results support the adequacy of the present calculations.

The PECs thus obtained are displayed in Figure 3. At the $^4A_{2g}$ geometry ($S = -3.93$ amu$^{1/2}$Å), the $^4T_{2g}$ state split into a $^4T_{2g}(^4A)$ and degenerate $^4T_{2g}(^4A)$ and $^4T_{2g}(^4B)$ states. As seen in Figure 3, the lowest energy $^4T_{2g}(^4A)$ state is stabilized as the geometry gets closer to the Jahn-Teller distorted $^4T_{2g}$ one ($S = 3.93$ amu$^{1/2}$Å), while the other two states show the opposite trend. This result indicates that the Jahn-Teller effect was successfully reproduced in both the DFT(B3LYP) and MCQDPT calculations. It was also confirmed at the DFT-optimized $^4T_{2g}$ geometry that the wave function of the lowest energy $^4T_{2g}(^4A)$ state is essentially represented by a single configuration $\left|d_{yz}d_{zx}d_{x^2-y^2}\right|$

as in the case of the DFT calculation in Sec. 2.1, indicating that the DFT calculation was adequate to optimize the Jahn-Teller distorted geometry.

We further evaluated the SOCs along the linear reaction path using the full Breit-Pauli Hamiltonian [36] and CASCI(3, 5) wave functions, which were constructed from the molecular orbitals optimized for the doublet states with the state-averaged CASSCF(3, 5) method. It should be pointed out that the optimized orbitals could describe the quartet state wave functions which have the correct symmetry and degeneracy. Because we focus on the ISC process from the lowest energy $^4T_{2g}(^4A)$ state as mentioned before, it is worthwhile to examine the SOCs involving this state at the potential crossing points. As seen in Figure 3, the lowest energy $^4T_{2g}(^4A)$ PEC crosses the three $^2T_{1g}$-derived ones at $S \approx -2.3$ amu$^{1/2}$Å and the $^2E_g(^2A)$ one at $S = -0.4$ amu$^{1/2}$Å. As listed in Table 2, the root-mean-squared SOCs with the former three states range from 100 to 170 cm^{-1} at their respective crossing points, while the SOC with the $^2E_g(^2A)$ state is small, 21 cm^{-1}. This implies that the ISC process may not be efficient through the latter coupling. In contrast, there is no crossing between the $^4T_{2g}(^4A)$ and the $^2E_g(^2B)$ PECs as seen in Figure 3. However, a relatively large SOC of 371 cm^{-1} was obtained between these two states at $S =$ 1.9 amu$^{1/2}$Å. Note that the SOC with the $^2E_g(^2A)$ state is particularly small, 21 cm^{-1}, because the main configurations in the CASCI(3, 5) wave functions differ by two electrons. On the other hand, the other SOCs are relatively large because most configurations differ by a single electron. See the Supplementary Content for detailed discussion.

3. Insights into ultrafast intersystem crossing through wavepacket dynamics

In this section, the relaxation process of $Cr^{III}(acac)_3$ is discussed on the basis of the PECs and SOCs obtained in Sec. 2.2 with the aid of excited-state wavepacket simulations. As a first step to elucidate the origins of the ultrafast ISC, we consider the nuclear motion only along the linear reaction path in Sec. 2.1 and neglect the kinetic couplings in the wavepacket simulations. The PECs in Figure 3 and the SOCs are thus the diabatic curves and the diabatic couplings, respectively.

As the initial wavepacket, the vibrational ground state of the $^4A_{2g}$ PEC was set onto the lowest energy $^4T_{2g}(^4A)$ one at the Franck-Condon region with an assumption of the constant transition dipole moment. Since each spin-free state is distinguished by the spin quantum number M_S, the total of 26 states were handled in the wavepacket simulations. The M_S number of the initially-populated state was set to $-3/2$, but the other choices ($-1/2$, $1/2$, and $3/2$) little affected the following discussion; see the Supplementary Content. In pseudo-spectral representation of the wavepacket, the Fourier grid Hamiltonian method [37] was employed with a grid space of $\Delta S = 0.04$ amu$^{1/2}$Å. The time propagation of the wavepacket was then performed with a time step of $\Delta t = 10^{-3}$ fs up to $t = 500$ fs. The time propagator employed was the following multiple-electronic-state evolution operator involving SOC-induced surface transition [38]:

$$\exp\left[-\frac{i}{\hbar}\hat{\boldsymbol{H}}\Delta t\right] \approx \hat{\boldsymbol{U}}^{\text{off-diag}} \exp\left[-\frac{i}{\hbar}\left(\hat{\boldsymbol{T}}+\hat{\boldsymbol{V}}\right)\Delta t\right]\hat{\boldsymbol{U}}^{\text{off-diag}}, \tag{2}$$

where

$$\hat{\boldsymbol{U}}^{\text{off-diag}} \equiv \hat{\boldsymbol{U}} \exp\left[-\frac{i}{2\hbar}\hat{\boldsymbol{U}}^{\dagger}\hat{\boldsymbol{V}}_{\text{SOC}}\hat{\boldsymbol{U}}\Delta t\right]\hat{\boldsymbol{U}}^{\dagger}. \tag{3}$$

The exponential term involving the diagonal kinetic and potential energy matrices, $\hat{\boldsymbol{T}}$ and $\hat{\boldsymbol{V}}$, in Eq. (2) was treated with the Chebyshev method [39]. The transformation matrix $\hat{\boldsymbol{U}}$ in Eq. (3) diagonalizes the SOC matrix, $\hat{\boldsymbol{V}}_{\text{SOC}}$, obtained in Sec. 2.2. In investigating the population change for each state, we added up the resulting populations of all possible M_S states.

Figure 4 shows the time-dependent population changes calculated from the wavepacket simulation, where ultrafast $^4T_{2g} \rightarrow {}^2T_{1g}$ ISC is observed: nearly 40% of the $^4T_{2g}(^4A)$ state undergoes ISC to the $^2T_{1g}$ states within 250 fs. On this time scale, the expectation value of the reaction coordinate $\langle S \rangle$ is not significantly deviated from the value of the $^4A_{2g}$ geometry, -3.93 amu$^{1/2}$Å, as shown in Figure 5. These results indicate that a notable fraction of the $^4T_{2g}$ population transfers into the $^2T_{1g}$ states before the wavepacket reaches to the Jahn-Teller distorted $^4T_{2g}$ geometry, though the reaction path S is the least motion path to this geometry. This ultrafast ISC can be understood by considering that the lowest energy $^4T_{2g}(^4A)$ and all $^2T_{1g}$ PECs cross near the Franck-Condon region as seen in Figure 3. Because the linear reaction path is mainly composed of the low-frequency modes as discussed in Sec. 2.1 and potential energy change should be small along such modes, these potential crossings are a consequence of near-degeneracy of the electronic states at the Franck-Condon region. The small distance between the Franck-Condon and the potential crossing regions is also demonstrated in Figure 5, where the $\langle S \rangle$ reaches to the crossing points

at -2.3 amu$^{1/2}$Å within 200 fs. Due to the potential crossings, the SOCs of 100$-$170 cm^{-1} in Table 2 are large enough to induce ISC.

In contrast to the ultrafast ISC to the $^2T_{1g}$ states, ISC to the ^2E_g states is not efficient as seen in Figure 4. The inefficient ISC to the $^2E_g(^2A)$ state is attributed to the smaller SOC of 21 cm^{-1} at the potential crossing point as discussed in Sec. 2.2. The ISC to the $^2E_g(^2B)$ state is also inefficient in spite of the larger SOC of 371 cm^{-1} at the small energy gap region. This inefficient ISC is attributed to the absence of potential crossings along the linear reaction path, which seems to emphasize the importance of potential crossings near the Franck-Condon region for the ultrafast ISC. Since the $^2T_{1g}$ and ^2E_g states are close in energy as seen in Figure 3, it is likely that fast internal conversion to the ^2E_g states will occur after the ultrafast $^4T_{2g}\rightarrow{}^2T_{1g}$ ISC observed in the present simulation. This is consistent with the experimental observations [1, 2], though more detailed studies considering the contribution from other vibrational degrees of freedom and from the kinetic couplings are desired to gain further understanding of the relaxation process of $Cr^{III}(acac)_3$.

4. Conclusions

We theoretically investigated the relaxation process from the initially-populated $^4T_{2g}$ state of $Cr^{III}(acac)_3$ through focusing on the structural relaxation of this state. The equilibrium geometries and the PECs obtained agreed well with the experimental ones. The ultrafast $^4T_{2g}\rightarrow{}^2T_{1g}$ ISC, observed in the wavepacket simulation, can be understood based on the PECs and the SOCs: the lowest

energy $^4T_{2g}(^4A)$ and all $^2T_{1g}$ PECs cross near the Franck-Condon region and the SOCs of 100−170 cm^{-1} are large enough to induce the ISC. Considering the importance of low-frequency modes, these potential crossings arise from near-degeneracy of electronic states in the Franck-Condon region.

Acknowledgements

The work was financially supported in part by Grant-in-Aid for Scientific Research on Priority Areas "Molecular Science for Supra Functional Systems"(477-22018016), Grant-in-Aid for Scientific Research on Innovative Areas "Molecular Science of Fluctuations"(2006-21107511, 23107714), as well as by Grant-in-Aid for Scientific Research (C) (20550013). All of them were supported by the Ministry of Education, Culture, Sports, Science and Technology (MEXT) Japan.

[1] E.A. Juban, J.K. McCusker, J. Am. Chem. Soc. 127 (2005) 6857.

[2] E.A. Juban, A.L. Smeigh, J.E. Monat, J.K. McCusker, Coord. Chem. Rev. 250 (2006) 1783.

[3] E.M.S. Maçôas, R. Kananavicius, P. Myllyperkiö, M. Pettersson, H. Kunttu, J. Am. Chem. Soc. 129 (2007) 8934.

[4] J.N. Schrauben, K.L. Dillman, W.F. Beck, J.K. McCusker, Chem. Sci. 1 (2010) 405.

[5] A. Steffen, M.G. Tay, A.S. Batsanov, J.A.K. Howard, A. Beeby, K.Q. Vuong, X.-Z. Sun, M.W. George, T.B. Marder, Angew. Chem. Int. Ed. 49 (2010) 2349.

[6] W. Gawelda, A. Cannizzo, V.-T. Pham, F. van Mourik, C. Bressler, M. Chergui, J. Am. Chem. Soc. 129 (2007) 8199.

[7] A. Cannizzo, A.M. Blanco-Rodríguez, A.E. Nahhas, J. Šebera, S. Záliš, A. Vlček, Jr., M. Chergui, J. Am. Chem. Soc. 130 (2008) 8967.

[8] G.S.M. Tong, P.K. Chow, C.-M. Che, Angew. Chem. Int. Ed. 49 (2010) 9206.

[9] B. Ordejón, C. de Graaf, C. Sousa, J. Am. Chem. Soc. 130 (2008) 13961.

[10] C. de Graaf, C. Sousa, Chem. Eur. J. 16 (2010) 4550.

[11] C. de Graaf, C. Sousa, Int. J. Quantum Chem. 111 (2011) 3385.

[12] T. Matsushita, T. Asada, S. Koseki, J. Phys. Chem. C 111 (2007) 6897.

[13] S. Koseki, T. Asada, T. Matsushita, J. Comput. Theor. Nanosci. 6 (2009) 1352.

[14] C. Daniel, M.-C. Heitz, J. Manz, C. Ribbing, J. Chem. Phys. 102 (1995) 905.

[15] M.-C. Heitz, C. Ribbing, C. Daniel, J. Chem. Phys. 106 (1997) 1421.

[16] H. Nakano, J. Chem. Phys. 99 (1993) 7983.

[17] A.D. Becke, J. Chem. Phys. 98 (1993) 5648.

[18] C. Lee, W. Yang, R.G. Parr, Phys. Rev. B: Condens. Matter 37 (1988) 785.

[19] B. Miehlich, A. Savin, H. Stoll, H. Preuss, Chem. Phys. Lett. 157 (1989) 200.

[20] A.D. Kirk, Chem. Rev. 99 (1999) 1607.

[21] N.B. Balabanov, K.A. Peterson, J. Chem. Phys. 123 (2005) 064107.

[22] T.H. Dunning, Jr., J. Chem. Phys. 90 (1989) 1007.

[23] M.J. Frisch *et al.*, Gaussian 03, Gaussian, Inc., Wallingford, CT, 2003.

[24] U. Varetto, Molekel 5.4, Swiss National Supercomputing Centre, Manno, Switzerland, 2009.

[25] W.H. Miller, B.A. Ruf, Y.-T. Chang, J. Chem. Phys. 89 (1988) 6298.

[26] C.-Y. Ng, T. Baer, I. Powis, Unimolecular and Bimolecular Ion-Molecule Reaction Dynamics, John Wiley & Sons, Chichester, 1994.

[27] B. Morosin, Acta Cryst. 19 (1965) 131.

[28] F. Duschinsky, Acta Physicochim. URSS 7 (1937) 551.

[29] M.W. Schmidt *et al.*, J. Comput. Chem. 14 (1993) 1347.

[30] K. Pierloot, E. Tsokos, B.O. Roos, Chem. Phys. Lett. 214 (1993) 583.

[31] Y.-K. Choe, Y. Nakao, K. Hirao, J. Chem. Phys. 115 (2001) 621.

[32] Y. Nakao, Y.-K. Choe, K. Nakayama, K. Hirao, Mol. Phys. 100 (2002) 729.

[33] H.A. Witek, Y.-K. Choe, J.P. Finley, K. Hirao, J. Comput. Chem. 23 (2002) 957.

[34] S. Sugano, Y. Tanabe, H. Kamimura, Multiplets of Transition-Metal Ions in Crystals, Academic Press Inc., New York, 1970.

[35] C. Ribbing, K. Pierloot, A. Ceulemans, Inorg. Chem. 37 (1998) 5227.

[36] D.G. Fedorov, S. Koseki, M.W. Schmidt, M.S. Gordon, Int. Rev. Phys. Chem. 22 (2003) 551.

[37] G.G. Balint-Kurti, C.L. Ward, C.C. Marston, Comput. Phys. Commun. 67 (1991) 285.

[38] T. Suzuki, H. Katayanagi, S. Nanbu, M. Aoyagi, J. Chem. Phys. 109 (1998) 5778.

[39] H. Tal-Ezer, R. Kosloff, J. Chem. Phys. 81 (1984) 3967.

Table 1: Selected geometrical parameters of equilibrium geometries of the $^4A_{2g}(^4B)$ ground state and the lowest energy $^4T_{2g}(^4A)$ state.[a] The numbering of atoms is defined in Figure 1.

	$^4A_{2g}$	$^4T_{2g}$	Δ[b]
Bond length (Å)			
$Cr - O^1$	1.975	1.958	−0.017
$Cr - O^2$	1.975	2.130	0.155
$Cr - O^3$	1.975	2.013	0.038
$Cr - O^4$	1.975	1.958	−0.017
$Cr - O^5$	1.975	2.013	0.038
$Cr - O^6$	1.975	2.130	0.155
Dihedral angle (deg.)			
$O^3 - O^4 - O^1 - O^5$	90.3	120.3	30.0

[a] The $^4A_{2g}$ and $^4T_{2g}$ geometries belong to the D_3 and C_2 point groups, respectively.

[b] The Δ values represent the differences between the $^4T_{2g}$ and the $^4A_{2g}$ geometry.

Table 2: Root-mean-squared spin-orbit coupling elements (SOCs) between a doublet and the lowest energy $^4T_{2g}(^4A)$ states.[a]

$\leftrightarrow {}^4T_{2g}({}^4A)$	SOC (cm^{-1})	S ($\mathrm{amu}^{1/2}$Å)[b]
$^2E_g(^2B)$	371	1.9
$^2E_g(^2A)$	21	−0.4
$^2T_{1g}(^2A)$	168	−2.4
$^2T_{1g}(^2B)$	147	−2.0
$^2T_{1g}(^2B)$	105	−2.4

[a] The listed SOC values are root-mean-square values for SOC matrix elements over all possible M_S states.

[b] The S values represent potential energy crossing points (or small energy gap region), at which the listed SOCs were evaluated.

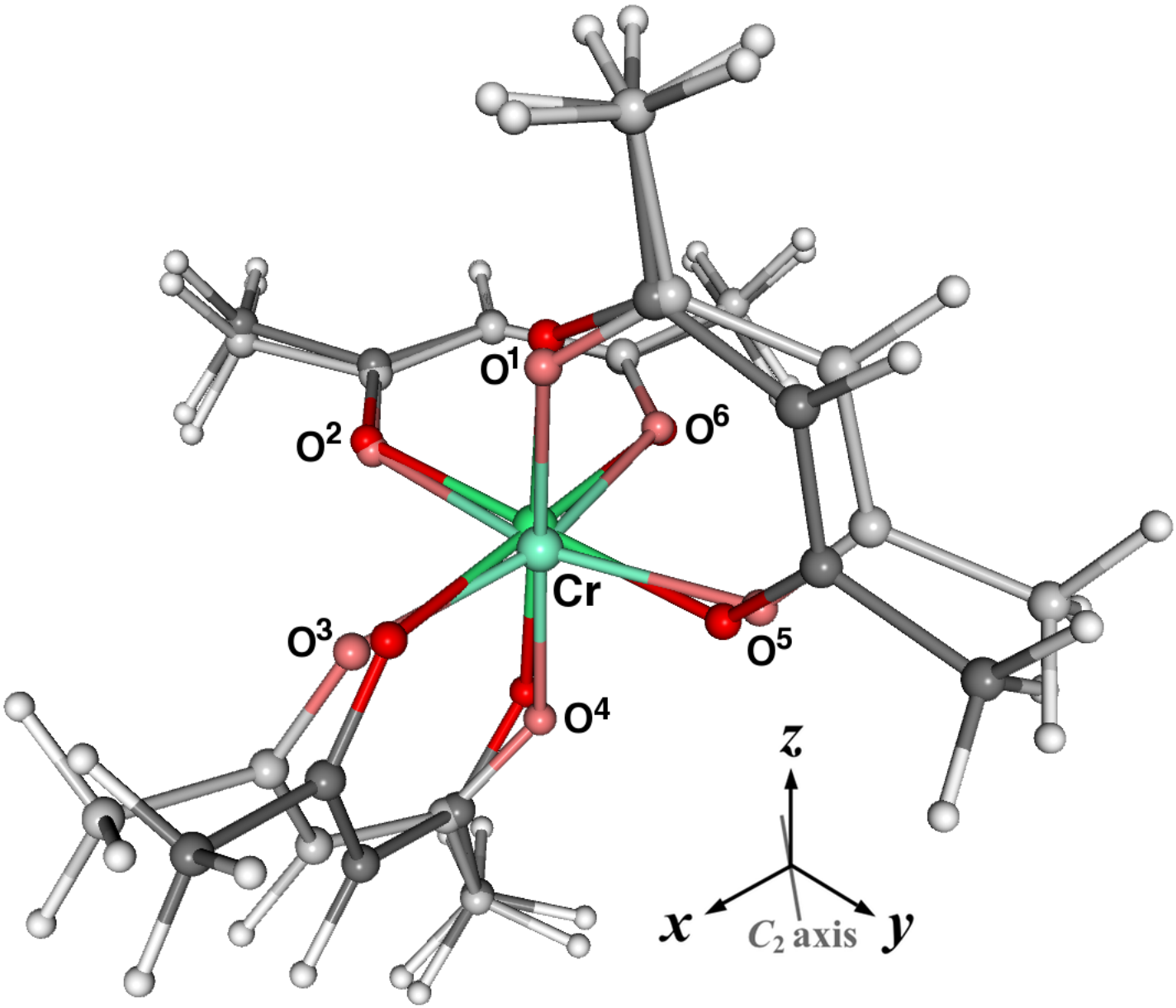

Figure 1: Equilibrium geometries of the ${}^4A_{2g}({}^4B)$ ground state (deep color) and the lowest energy ${}^4T_{2g}({}^4A)$ state (light color). The two geometries are positioned so as not to generate any linear or angular momentum. The C_2 axis is aligned with the bisector between the x and y axes.

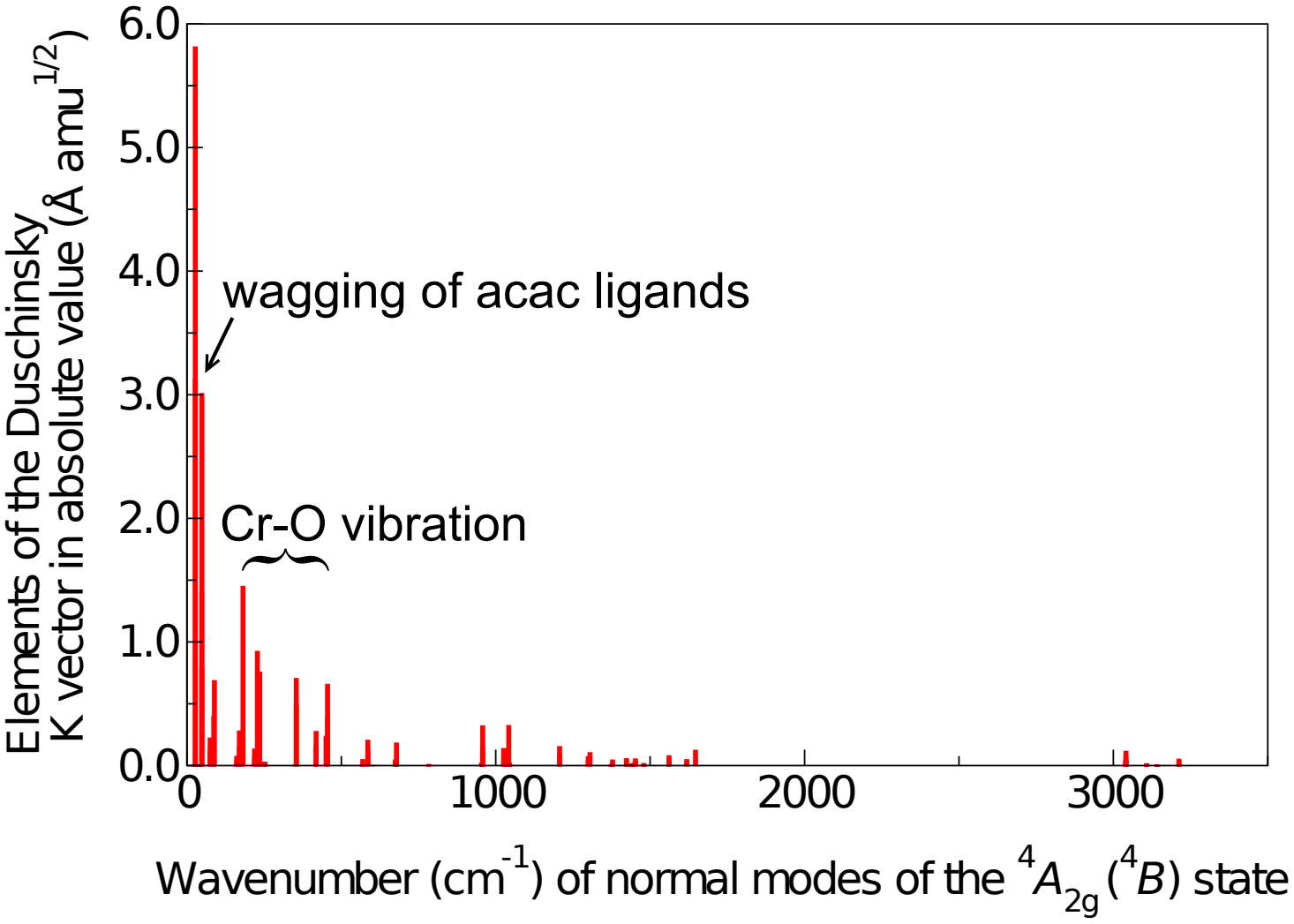

Figure 2: Decomposition of the displacement between the $^4T_{2g}$ and the $^4A_{2g}$ geometry in terms of the $^4A_{2g}$ normal modes.

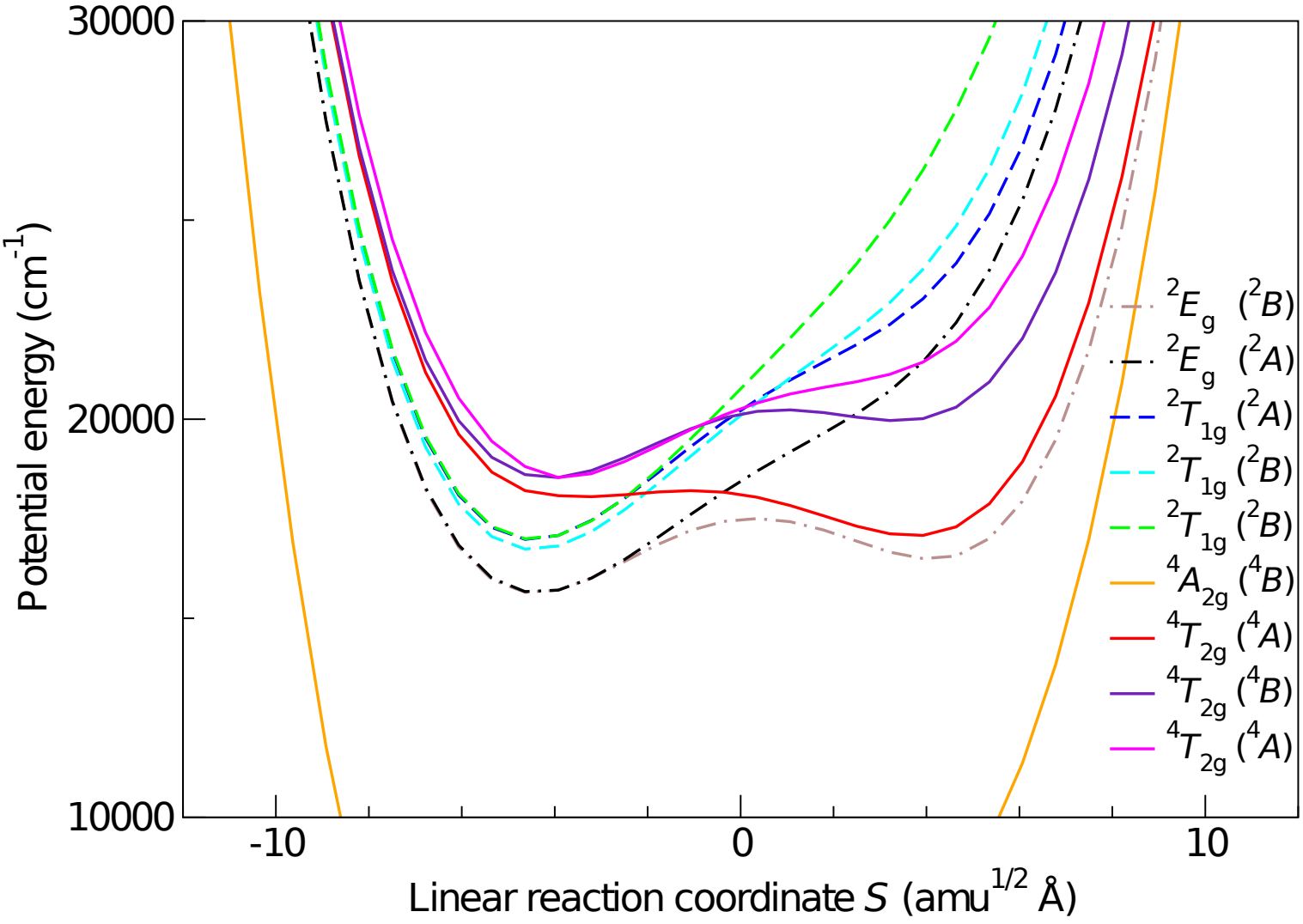

Figure 3: Potential energy curves of low-lying electronic states along the linear reaction path S. The electronic states are classified by irreducible representations of the $O_h(C_2)$ point group. The $^4A_{2g}$ and $^4T_{2g}$ geometries correspond to -3.93 and 3.93 amu$^{1/2}$Å, respectively. The energy of the $^4A_{2g}$ state at its equilibrium geometry is set to be zero.

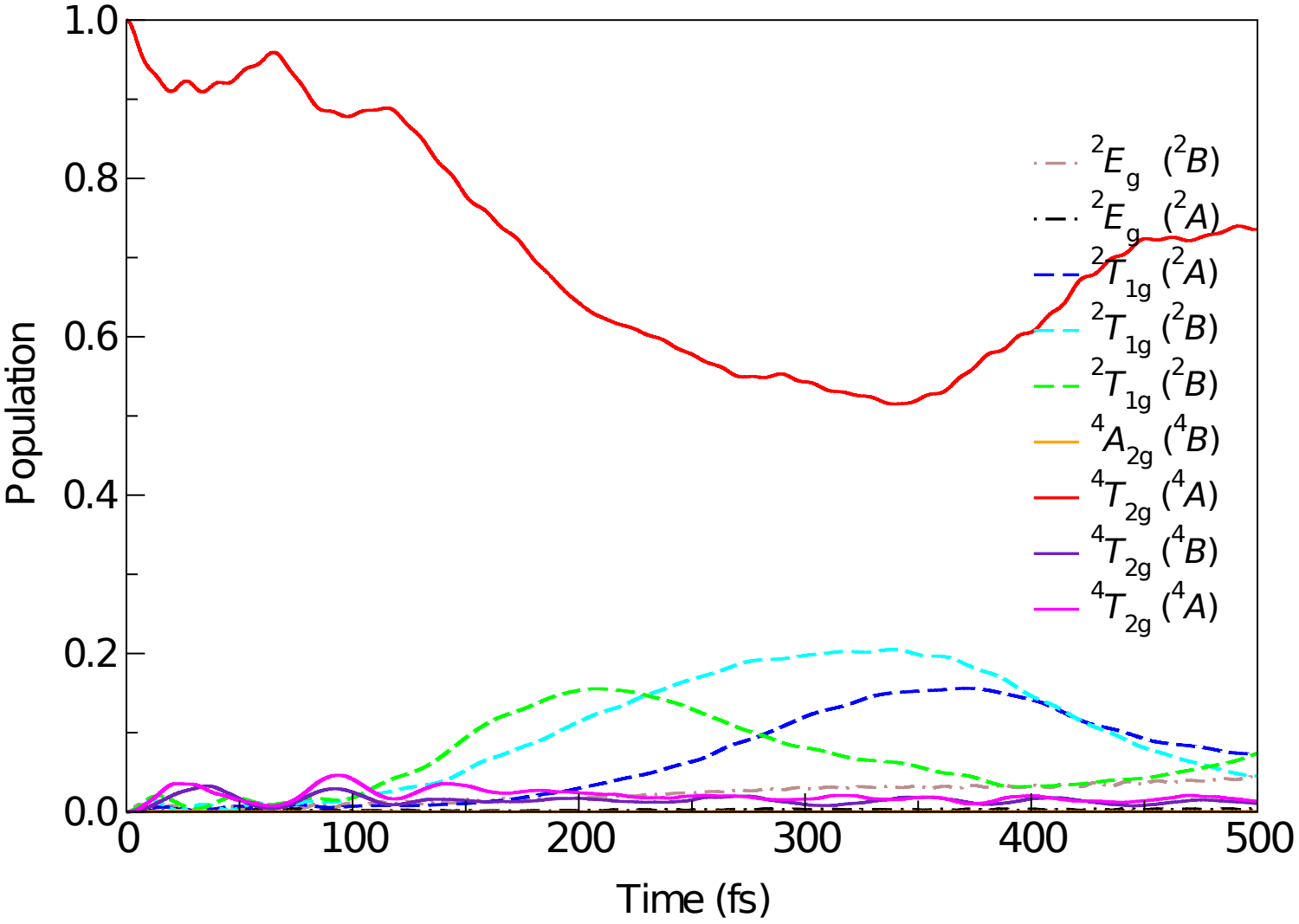

Figure 4: Population change on each electronic state. The initial wavepacket was set on the lowest energy $^4T_{2g}(^4A)$ PEC whose $M_S = -3/2$.

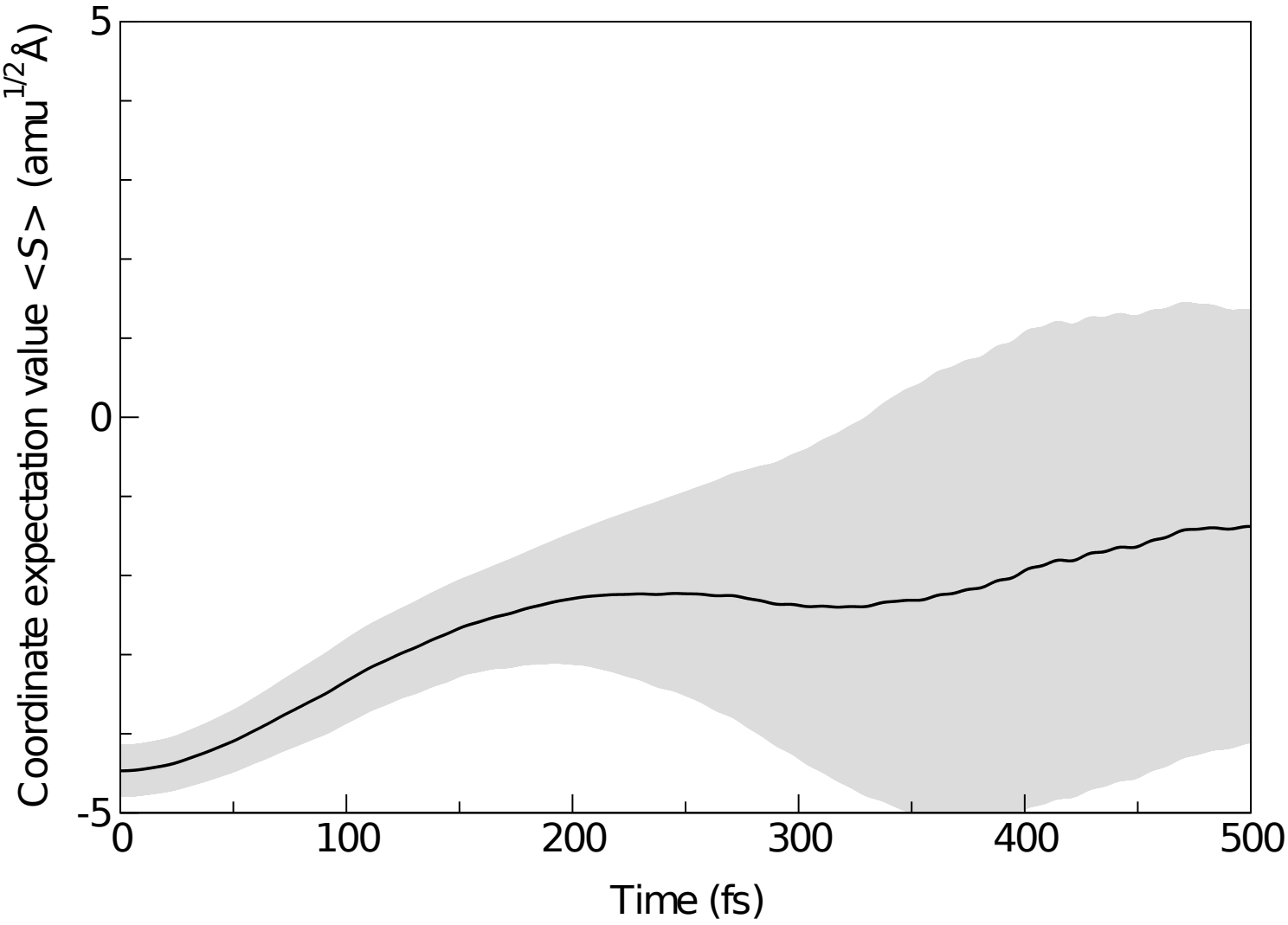

Figure 5: Expectation value of coordinate S (black solid line) with standard deviation (gray region) for the wavepacket on the lowest energy ${}^4T_{2g}({}^4A)$ PEC whose $M_S = -3/2$. The ${}^4A_{2g}$ and ${}^4T_{2g}$ geometries correspond to -3.93 and 3.93 amu$^{1/2}$Å, respectively.